



High-resolution [O I] Line Spectral Mapping of TW Hya Consistent with X-Ray-driven Photoevaporation

Christian Rab^{1,2}, Michael L. Weber^{1,3}, Giovanni Picogna¹, Barbara Ercolano^{1,3}, and James E. Owen⁴¹ University Observatory, Faculty of Physics, Ludwig-Maximilians-Universität München, Scheinerstr. 1, D-81679 Munich, Germany; rab@mpe.mpg.de² Max-Planck-Institut für extraterrestrische Physik, Giessenbachstrasse 1, D-85748 Garching, Germany³ Exzellenzcluster "Origins," Boltzmannstr. 2, D-85748 Garching, Germany⁴ Astrophysics Group, Imperial College London, Blackett Laboratory, Prince Consort Road, London SW7 2AZ, UK

Received 2023 August 11; revised 2023 August 28; accepted 2023 August 30; published 2023 September 20

Abstract

Theoretical models indicate that photoevaporative and magnetothermal winds play a crucial role in the evolution and dispersal of protoplanetary disks and affect the formation of planetary systems. However, it is still unclear what wind-driving mechanism is dominant or if both are at work, perhaps at different stages of disk evolution. Recent spatially resolved observations by Fang et al. of the [O I] 6300 Å spectral line, a common disk wind tracer in TW Hya, revealed that about 80% of the emission is confined to the inner few astronomical units of the disk. In this work, we show that state-of-the-art X-ray-driven photoevaporation models can reproduce the compact emission and the line profile of the [O I] 6300 Å line. Furthermore, we show that the models also simultaneously reproduce the observed line luminosities and detailed spectral profiles of both the [O I] 6300 Å and the [Ne II] 12.8 μm lines. While MHD wind models can also reproduce the compact radial emission of the [O I] 6300 Å line, they fail to match the observed spectral profile of the [O I] 6300 Å line and underestimate the luminosity of the [Ne II] 12.8 μm line by a factor of 3. We conclude that, while we cannot exclude the presence of an MHD wind component, the bulk of the wind structure of TW Hya is predominantly shaped by a photoevaporative flow.

Unified Astronomy Thesaurus concepts: [Protoplanetary disks \(1300\)](#); [Computational astronomy \(293\)](#); [Classical T Tauri stars \(252\)](#)

1. Introduction

The evolution and final dispersal of protoplanetary disks are thought to strongly affect the formation and evolution of planetary systems. Disk winds are considered to be significant contributors to the evolutionary processes occurring within protoplanetary disks (Lesur et al. 2023; Pascucci et al. 2023). Thermal winds can be launched through photoevaporation (PE) from the central star (e.g., Gorti & Hollenbach 2009; Nakatani et al. 2018; Ercolano et al. 2021; Picogna et al. 2021) and are efficient at removing material at rates comparable to the observed accretion rates of T-Tauri stars (e.g., Ercolano & Pascucci 2017). Thermal winds do not remove angular momentum from the disk, and, when combined with viscous accretion models, they are successful in reproducing the observed two-timescale behavior, evidenced by the evolution of disk colors (e.g., Koepferl et al. 2013; Ercolano et al. 2015) and several observational correlations such as the observed accretion rates and the mass of the central star (Ercolano et al. 2014) or inner disk life times (Picogna et al. 2021).

The inclusion of nonideal magnetohydrodynamical effects in a weakly ionized protoplanetary disk has shown that magnetorotational instability (MRI; Balbus & Hawley 1991), hypothesized to drive viscosity in disks, is suppressed in most regions of the disk (see, e.g., Lesur et al. 2023, for a recent review), except the very inner regions where thermionic emission from dust dominates (Desch & Turner 2015; Jankovic et al. 2021). Vigorous, magnetically supported disk winds (from now on MHD winds) are a solid prediction of most

recent simulations (e.g., Gressel et al. 2015, 2020; Bai et al. 2016; Wang et al. 2019; Lesur 2021) and they replace MRI in most disk regions by removing angular momentum from the disk, allowing the material to flow inward.

Which type of wind might dominate at different times and different locations in a disk is an important question that directly affects planet formation models. The current picture emerging from the careful analysis of spectroscopic diagnostics is that both types of winds operate in disks, with MHD winds stronger in young objects and thermal winds dominating the final evolution and eventual dispersal of disks (Ercolano & Pascucci 2017; Weber et al. 2020).

Currently used spectroscopic wind diagnostics, particularly the [O I] 6300 Å collisionally excited spectral line, have complex line profiles (e.g., Simon et al. 2016; Fang et al. 2018; Banzatti et al. 2019; Gangi et al. 2020), often preventing important wind parameters, such as the wind launching radius, to be directly determined (see the discussion in Weber et al. 2020). Rab et al. (2022) find that a combination of [O I] 6300 Å and molecular hydrogen observations are consistent with thermal winds driven by X-ray PE, but alternative models cannot be ruled out.

In order to break the degeneracies hidden in the interpretation of nonspatially resolved line profiles, high-resolution spectral mapping of wind diagnostics represents an attractive option. This has recently been done for the [O I] 6300 Å line from TW Hya by Fang et al. (2023), using the multiunit spectroscopic explorer (MUSE) at the Very Large Telescope, who showed that about 80% of the [O I] emission is confined to within 1 au radially from the star. In this paper, we show that state-of-the-art thermal wind models driven by X-ray PE (e.g., Picogna et al. 2019, 2021; Ercolano et al. 2021) are consistent with the observations recently published by Fang et al. (2023). In Section 2 we briefly describe the used photoevaporative disk



Original content from this work may be used under the terms of the [Creative Commons Attribution 4.0 licence](#). Any further distribution of this work must maintain attribution to the author(s) and the title of the work, journal citation and DOI.

wind models and our approach to produce synthetic observables. In Section 3 we show our results, in particular the comparison to the observational data. We discuss our results in context to previous works and MHD disk wind models and present our conclusions in Section 4.

2. Methods

In this section, we describe the physical models used in this work and how we produce synthetic observables from those models that can be directly compared to observational data.

2.1. Photoevaporative Disks Wind Models

To model a photoevaporative disk wind we follow the approach by Picogna et al. (2019, 2021) and Ercolano et al. (2021),⁵ to which we refer for details. This model uses a modified version of the PLUTO code (Mignone et al. 2007; Picogna et al. 2019) to perform radiative-hydrodynamic simulations of a disk irradiated by a central star. The temperatures in the wind and the wind-launching regions, i.e., the upper layers of the disk, where the column number density toward the central star is in the range between 5×10^{20} and $2.5 \times 10^{22} \text{ cm}^{-2}$, are determined by parameterizations that are derived from detailed radiative transfer calculations with the gas photoionization code MOCASSIN (Ercolano et al. 2003, 2005, 2008). For a given column number density, the respective parameterization yields the gas temperature dependent on the ionization parameter $\xi = \frac{L_X}{nr^2}$, where L_X is the X-ray luminosity of the star, n is the volume number density, and r is the spherical radius. In this work, we use a stellar mass $M_* = 0.7M_\odot$ and the parameterizations derived from the spectrum labeled as Spec29 in Ercolano et al. (2021) with $L_X = 2 \times 10^{30} \text{ erg s}^{-1}$, which is appropriate considering observational constraints on TW Hya (Robrade & Schmitt 2006; Ercolano et al. 2017). The computational grid was centered on the star. Spherical polar coordinates were adopted with 512 logarithmic spaced cells in the radial direction from 0.33 to 600 au, and 512 uniform spaced cells in the polar one from 0.005 to $\pi/2$. Outflow boundaries were adopted in the radial directions, while special reflective boundaries were used to treat the regions close to the polar axis and the disk midplane. A periodic boundary was assumed in the azimuthal direction. The influence of the inner boundary was tested by decreasing the inner radial boundary to 0.1 au, while keeping the same radial resolution outside 0.33 au.

2.2. Disk Model without a Wind

In addition to the PE disk wind models, we use an existing radiation thermochemical disk model for TW Hya from the DIANA (DIsc ANalysis)⁶ project presented in Woitke et al. (2019). This model does not include a wind component but was made to reproduce existing (mostly spatially unresolved) observational data, including the spectral energy distribution and about 50 spectral lines (i.e., line fluxes are matched within a factor of 2 to 3). With this model, we show how a pure disk model compares with the spatially resolved [O I] 6300 Å observations. As at the time of the publication of this model no spatially resolved observables for the [O I] 6300 Å were

produced, we rerun the model with a more recent version of the radiation thermochemical code PRODiMO (PROtoplanetary DIsk MOdel⁷, Woitke et al. 2009; Kamp et al. 2010; Thi et al. 2011; Woitke et al. 2016) to produce line cubes and images that can be compared to the spatially resolved data.

2.3. Synthetic Observables

To produce synthetic observables we use two different approaches to postprocess the PE disk wind model. Similar to Weber et al. (2020), we use the MOCASSIN Monte Carlo radiative transfer code that allows us to model spectral line emission for atomic species in the optical and infrared (Ercolano et al. 2003, 2005, 2008). Furthermore, we use the radiation thermochemical code PRODiMO that was recently applied in Rab et al. (2022) to produce synthetic observables for atomic and molecular species that are supposed to trace disk winds. We use both approaches to show that our results, in particular the spatial extent of the [O I] 6300 Å, are robust and do not strongly depend on the details of the postprocessing method (e.g., chemistry, heating-cooling, and line excitation).

For both approaches, we use the same physical structure (density and velocity field), the same X-ray/stellar spectrum, and the same dust properties. To account for the accretion luminosity, we add to the X-ray spectrum a blackbody spectrum with $T_{\text{eff}} = 12,000 \text{ K}$ normalized to $L_{\text{acc}} = 2.95 \times 10^{-2} L_\odot$ (Fang et al. 2018). For the dust, we assume a gas-to-dust ratio of 100 and interstellar medium size distribution (see Weber et al. 2020 for details). Quantities such as temperatures, line populations, chemical abundances, and synthetic observables are self-consistently calculated within each postprocessing framework. For a more detailed discussion on these different postprocessing approaches and a comparison, see Rab et al. (2022).

At first, we use the line radiative transfer modules of MOCASSIN and PRODiMO to produce synthetic model images for the [O I] 6300 Å emission assuming a distance of 60 pc (Gaia Collaboration et al. 2021) and a disk inclination of 7° (Qi et al. 2004), consistent with Fang et al. (2023). For the produced model images, we use an oversampling factor of 7 (0.003615) compared to the pixel scale of the observations. Following Fang et al. (2023), we downsample the model images to the pixel scale of the MUSE data before convolving it with the point-spread function (PSF). For these model images and for the observed image, we produce azimuthally averaged radial profiles using the corresponding pixel scale as the width for the radial bins. Additionally, we also produce radial profiles for the unconvolved model images to better show the real extent of the emission. We also produce synthetic images in the same way for the toy model (power-law model) presented in Fang et al. (2023) and the thermochemical model without a wind. We note that the used oversampling factor is not enough to fully resolve the toy model of Fang et al. (2023), but we found that it is sufficient to reproduce the observation after convolution of the toy model image (mainly because a downsampling to the pixel size of the observations is required anyway). We also note that a higher resolution spatial grid is used for the radiative transfer step, but as we are not aiming for a detailed fitting of the observational data we use the oversampling factor of all model images for consistency (e.g., between the two different postprocessing methods) and efficiency.

⁵ X-ray PE models and data from Picogna et al. (2021) are available here: <https://cutt.ly/IEIY9JI>.

⁶ <https://diana.iwf.oeaw.ac.at>

⁷ <https://prodimo.iwf.oeaw.ac.at> revision: 66efbd75 2023 June 27.

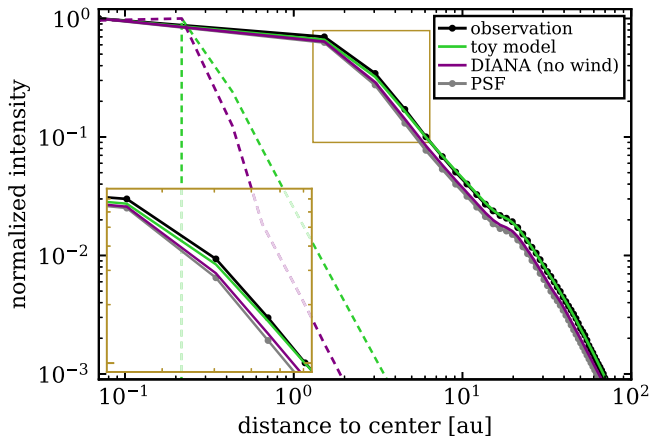


Figure 1. The toy (power-law) model (green) from Fang et al. (2023) compared to results from a radiation thermochemical disk model (purple) without a wind that fits a large set of observational data for TW Hya (Woitke et al. 2019). The dashed and solid colored lines show the radial profiles for the unconvolved and convolved images, respectively. The gray solid line shows the radial profile of the PSF and the black solid line for the [O I] 6300 Å MUSE observations (Fang et al. 2023). The inset shows a zoom-in to the region marked by the brown box ($r = 1.3\text{--}6.4$ au) in the main panel.

We also compare our model with the observations of the [Ne II] 12.8 μm line presented in Pascucci et al. (2011). For this line, we simply produce spectral line profiles, again using both postprocessing approaches.

3. Results

Here, we compare our modeling results to the observational data. As we do not present newly developed PE models, we focus only on the observables. In Section 3.1 we present normalized azimuthally averaged radial profiles for [O I] 6300 Å in a similar fashion as Fang et al. (2023), and in Section 3.2 we compare our PE wind models to the observed spectral profiles for the [O I] 6300 Å and [Ne II] 12.8 μm spectral lines.

3.1. Radial Profiles

3.1.1. Disk-only Model

In Figure 1, we show the toy model from Fang et al. (2023) in comparison to the disk-only model from Woitke et al. (2019). The thermochemical disk model shows a similar radial profile for the [O I] 6300 Å emission, in particular the steep slope, but is slightly more compact and hence does not match the data (i.e., it remains unresolved). We note that the model of Woitke et al. (2019) uses a parameterized disk structure, which is quite different to the disk wind models used in this work or in Fang et al. (2023), in particular, it has a dust- and gas-depleted (optically thin but not empty) inner hole extending up to almost 3 au. Although it is possible to adapt this model to achieve a better match to the spatially resolved data, such a disk-only model, by construction, cannot match the blueshifts seen in the observed line profiles of the [O I] 6300 Å and [Ne II] 12.8 μm lines. Nevertheless, it is interesting to see that such a model is almost in agreement with the spatially resolved data, although such constraints were not included in the modeling. Furthermore, this model indicates that a disk-only solution seems to produce an even more compact emission region for the [O I] 6300 Å compared to the wind models presented here or

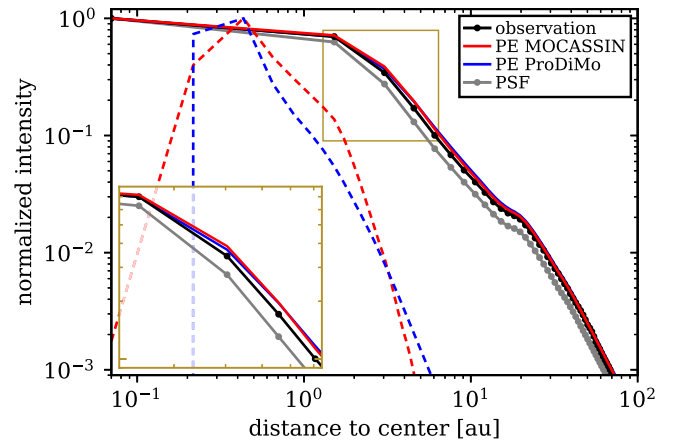


Figure 2. Comparison of the photoevaporative disk wind model with the observed normalized radial intensity profiles of the [O I] 6300 Å line. The black solid line shows the observation, and the gray solid line shows the PSF (both from Fang et al. 2023). The colored solid and dashed lines show the model results, convolved with the PSF and at the resolution of the model image, respectively. In red, we show the results from the MOCASSIN and in blue from the PRODIMO postprocessing. The inset shows a zoom-in to the region marked by the brown box ($r = 1.3\text{--}6.4$ au) in the main panel.

in Fang et al. (2023) and also that the contribution from a disk itself can be significant in the case of TW Hya.

3.1.2. Photoevaporative Disk Wind Models

In Figure 2 we compare the [O I] 6300 Å radial intensity profiles of our PE wind model at an inclination of 7° to the observation by Fang et al. (2023). As can be seen in the unconvolved radial profiles, both the MOCASSIN and PRODIMO models yield very similar results, with the PRODIMO model having slightly more emission at very low ($\lesssim 0.4$ au) and at extended radii, and MOCASSIN showing enhanced emission at intermediate radii between ≈ 0.5 and 3 au. In both models, the emission peaks well inside of 1 au with a steep decrease in intensity at larger radii. Computing the cumulative integral, we find that 80% of the emission originates inside 2 au of the central star, compared to 1 au for the toy model that Fang et al. (2023) derived as a fit to the data. This is also visible in Figure 3, where we show 2D emission maps overlain by contours showing the 80% regions. It is worth pointing out that although the 80% regions extend to ≈ 2 au and ≈ 14 au for the [O I] 6300 Å and [Ne II] 12.8 μm lines, respectively, the emission inside this region is not uniform but has a strong gradient with the peak close to the star. Comparing the profiles after convolution with the PSF, it can be seen that the radial profiles of the PE wind model are in very good agreement with the observations. This shows that current state-of-the-art photoevaporative disk models produce compact emission consistent with the spatially resolved observations of TW Hya.

Figure 3 shows significant emission originating from the inner 1 au, which is inside the gravitational radius of the X-ray PE models shown here (~ 3.5 au). The emitting material close to the star is thus bound to the inner disk and not affected by PE. This implies that our main result would not qualitatively change in the case of a “gapped” inner disk, as suggested by the observations of a dark annulus in millimeter-wave dust emission at ≈ 1 au (Andrews et al. 2016). Indeed, the presence of gas close to the central star of TW Hya, which shows clear accretion signatures, justifies the employment of primordial disk models in this case. While we do not expect significant changes to the wind structure due to the gap and hence on the

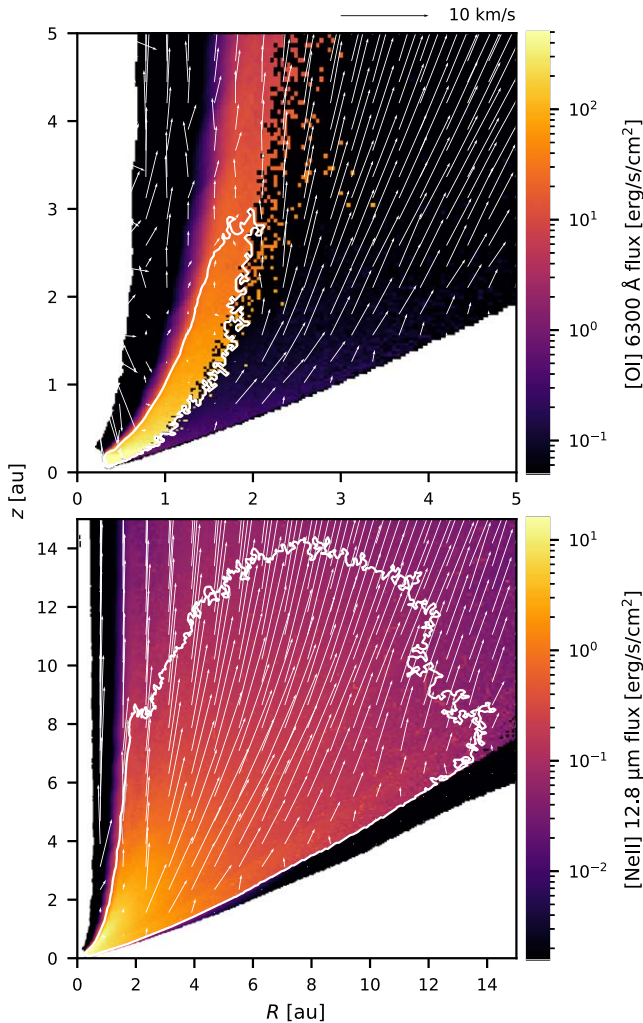


Figure 3. [O I] 6300 Å (top) and [Ne II] 12.8 μm (bottom) line flux of our PE disk wind model obtained by multiplying the emissivity with $2\pi R$ in order to illustrate the origin of the emission. White solid contour lines indicate the regions where the top 80% of emission originates. White arrows represent the velocity field in the PE model.

main picture of having compact emission, a detailed hydrodynamical model would be required to assess potential differences in the detailed spectroscopic line profiles emitted from this region (see also Section 4). Such a model is, however, outside the scope of this study and would also require higher spatial resolution in the observations of the inner disk, which is not possible with current instrumentation.

3.2. Spectral Line Profiles

In Figure 4 we compare the modeled spectral line profiles to the observations of the [O I] 6300 Å and [Ne II] 12.8 μm spectral lines. For [O I] 6300 Å, we show three different observed spectra representing the scatter observed in the measured centroid velocities v_c with a mean of $v_c = -0.8 \text{ km s}^{-1}$ and a standard deviation of 0.4 km s^{-1} (Fang et al. 2023). Both models are in good agreement with the observations. In particular the MOCASSIN ($v_c \approx -0.8 \text{ km s}^{-1}$) model matches the profile of Simon et al. (2016), which shows $v_c \approx -0.8 \text{ km s}^{-1}$ exceptionally well. The PRODIMO profile is slightly broader in the blue part of the spectrum and therefore appears more blueshifted ($v_c \approx -1.5 \text{ km s}^{-1}$). Nevertheless, this is still consistent with

observations, as, for example, the profile of Fang et al. (2023) shows a similar behavior with $v_c \approx -1.5 \text{ km s}^{-1}$ for the spectrum downgraded to $R = 40,000$. The [O I] 6300 Å line fluxes from the models are $1.2 \times 10^{-5} L_\odot$ (MOCASSIN) and $5.5 \times 10^{-6} L_\odot$ (PRODIMO), which is in good agreement with the observed values of $1.0\text{--}1.5 \times 10^{-5} L_\odot$ (Simon et al. 2016; Fang et al. 2018, 2023).

The difference in the shape of the two model spectra can be explained by the slightly more extended [O I] 6300 Å emission of the PRODIMO model (see Figure 2), which traces slightly faster velocities of the PE wind compared to the MOCASSIN model. We tested this by simply removing all emission for $r > 4 \text{ au}$ in the synthetic observables of the PRODIMO model and found that for this case the MOCASSIN and PRODIMO line profiles become almost identical. As the density structure and velocity fields in both models are the same, the differences arise from different radial temperature gradients and differences in the line excitation calculations. However, our results indicate that detailed models for TW Hya, fully considering the stellar properties and possibly also details of the disk structure (i.e., a gap in the disk structure; see Owen 2011), are required for a comprehensive interpretation of the [O I] 6300 Å line profile.

For [Ne II] 12.8 μm , the modeled profiles are very similar and match very well the observed spectral profile. As [Ne II] 12.8 μm traces regions further out and higher up (up to $r \approx 10 \text{ au}$) in the disk/wind with respect to [O I] 6300 Å, it traces higher velocities of the photoevaporative flow (see Figure 3), consistent with the observed $v_c \approx -5 \text{ km s}^{-1}$. The line luminosity of the models is $3.4 \times 10^{-6} L_\odot$ (MOCASSIN) and $5.1 \times 10^{-6} L_\odot$ (PRODIMO), which are in excellent agreement with the observed range of luminosities of $\approx 3.5\text{--}6.2 \times 10^{-6} L_\odot$ (Pascucci & Sterzik 2009; Najita et al. 2010; Pascucci et al. 2011).

4. Discussion and Conclusions

Our results show that current state-of-the-art PE disk wind models are consistent with the observational data presented in Fang et al. (2023). We want to emphasize that for this work we did not use any new developments or adaptations to the PE wind modeling approach already presented and used in Picogna et al. (2019, 2021), Weber et al. (2020, 2022), Ercolano et al. (2021), and Rab et al. (2022). The only difference between this work and previously published work is the choice of an appropriate X-ray spectrum for TW Hya.

Fang et al. (2023) compared the spatially resolved [O I] 6300 Å emission to very low-resolution early PE models (Ercolano & Owen 2010; Owen et al. 2010), which present a more extended emission profile for the [O I] 6300 Å. Based on this comparison, they concluded that a magnetothermal-driven wind is necessary to explain the spatially resolved [O I] 6300 Å line data. We show here, however, that, compared to the fiducial magnetothermal wind model presented in Fang et al. (2023), modern PE models produce only very slightly more extended [O I] 6300 Å emission but are still fully consistent with the data. Apart from the higher inner grid resolution, an important difference between the “old” PE models (Ercolano & Owen 2010; Owen et al. 2010) and the newer PE models (Picogna et al. 2019, 2021; Weber et al. 2020; Ercolano et al. 2021) is the temperature parameterization. The new models take into account the detailed column density distribution (attenuation) in the simulation regions, yielding a more accurate temperature (and thus density) profile. More specifically, the density in the inner disk is higher for the new models, resulting in a more compact emission region.

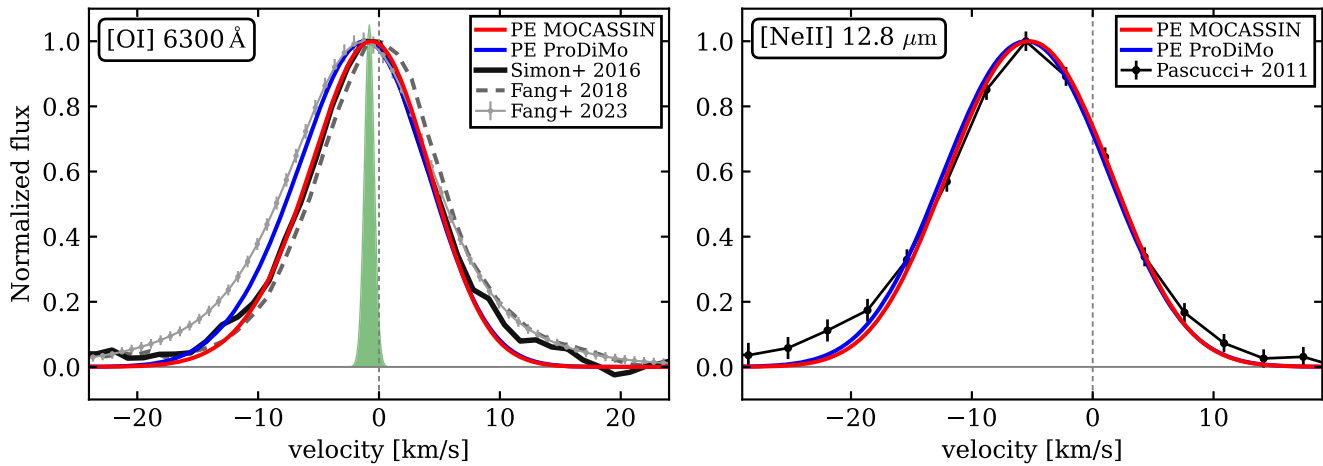


Figure 4. Comparison of observed [O I] 6300 Å (Simon et al. 2016; Fang et al. 2018, 2023) and [Ne II] 12.8 μm (Pascucci et al. 2011) spectral line profiles to synthetic line profiles of photoevaporative disk wind models. The [O I] line profiles from the models and that observed by Fang et al. (2023) have been degraded to a resolving power $R = 40,000$, comparable to the resolution in the observation by Simon et al. (2016). For the Fang et al. (2023) data, the error bars correspond to 3σ uncertainties (for visibility). The Gaussian distribution shown in green represents the derived mean centroid shift of -0.8 km s^{-1} with a standard deviation of 0.4 km s^{-1} as derived by Fang et al. (2023) from various observations of [O I] 6300 Å. The [Ne II] model profile has been degraded to $R = 30,000$ and the error bars in the observed profile indicate 1σ uncertainties.

The new PE models can match the observed line luminosity and the shape of the [O I] 6300 Å profile very well, in particular the small observed blueshift of $v_c \approx -0.8 \text{ km s}^{-1}$. As noted by Fang et al. (2023), the [O I] 6300 Å spectral profile of their MHD model is too blueshifted compared to observations, which is likely caused by the higher wind velocities in the inner regions compared to our PE model. Fang et al. (2023) argue that the discrepancy could be caused by the lack of an inner hole in their primordial disk model and that the presence of such a hole would allow for redshifted emission from the back side of the disk to contribute to the line profile, reducing its blueshift. However, in order to zero the velocity center by this effect, the line would then still be broadened by the blueshifted value (Ercolano & Owen 2010, 2016), which would then again be in tension with the observations. Additionally, as TW Hya is seen almost face-on, the contribution from the back side of the disk will be limited unless an unsuitable large inner hole (several astronomical units) is assumed. More quantitatively speaking, our model has an inner radius of $r_{\text{in}} = 0.33 \text{ au}$ (i.e., larger than the MHD model), but still, the back side of the disk contributes to less than 2% to the total flux and does not have any significant impact on the centroid velocity. We also tested a PE wind model with $r_{\text{in}} = 0.1 \text{ au}$ and found no significant differences. In any case, for a more thorough interpretation of the [O I] 6300 Å spectral profile of TW Hya, a more detailed disk structure model for the inner few astronomical units is required. In particular, constraints from Atacama Large Millimeter/submillimeter Array observations (gap at $\approx 1 \text{ au}$ and unresolved emission from $r < 0.5 \text{ au}$; Andrews et al. 2016) and Very Large Telescope/SPHERE (marginal detection of emission from the inner few astronomical units; van Boekel et al. 2017) indicate that there is likely still some dust in the inner 1–2 au (see also Ercolano et al. 2017) that would reduce [O I] 6300 Å emission from the back side of the disk.

As already noted in Pascucci et al. (2011) and also discussed in Fang et al. (2023), the [Ne II] 12.8 μm line observation points toward a thermally driven wind. This is supported by the models presented in this work, as the agreement of the PE wind model with the spectral line profile and the observed line fluxes (which is underpredicted by a factor of 3 by the MHD model of Fang et al. 2023) is excellent, indicating that at least for the

radii larger than a few astronomical units, traced by the [Ne II] 12.8 μm line, the disk wind structure of TW Hya is predominantly shaped by a PE flow.

We conclude that, while the currently available spatially resolved data does not allow us to clearly distinguish a pure thermally driven wind from a magnetothermal wind, the simultaneous agreement of the PE wind models with the spatially resolved data and the spectral profiles of [O I] 6300 Å and [Ne II] 12.8 μm strongly indicates that at least large parts of the disk wind seen in TW Hya are driven by X-ray PE.






Acknowledgments

We thank the anonymous referee for a quick and constructive report. We thank Min Fang for providing the reduced observational data for the [O I] 6300 Å line including the PSF. We acknowledge the support of the Deutsche Forschungsgemeinschaft (DFG, German Research Foundation) Research Unit “Transition discs”—325594231. This research was supported by the Excellence Cluster ORIGINS, which is funded by the Deutsche Forschungsgemeinschaft (DFG, German Research Foundation) under Germany’s Excellence Strategy—EXC-2094-390783311. C.H.R. is grateful for support from the Max Planck Society. This research has made use of NASA’s Astrophysics Data System. J.E.O. is supported by a Royal Society University Research Fellowship. J.E.O. has also received funding from the European Research Council (ERC) under the European Union’s Horizon 2020 research and innovation programme (Grant agreement No. 853022, PEVAP). For the purpose of open access, the authors have applied a Creative Commons Attribution (CC-BY) licence to any Author Accepted Manuscript version arising.

Software: This research made use of Astropy, a community-developed core Python package for Astronomy (Astropy Collaboration et al. 2013, 2018). This research made use of Photutils, an Astropy package for the detection and photometry of astronomical sources (Bradley et al. 2022). matplotlib version 3.7.0⁸ (Hunter 2007); scipy (Virtanen et al. 2020); numpy (Harris et al. 2020).

⁸ <https://doi.org/10.5281/zenodo.7637593>

ORCID iDs

Christian Rab  <https://orcid.org/0000-0003-1817-6576>
 Michael L. Weber,  <https://orcid.org/0000-0002-4983-0422>
 Giovanni Picogna  <https://orcid.org/0000-0003-3754-1639>
 Barbara Ercolano  <https://orcid.org/0000-0001-7868-2740>
 James E. Owen  <https://orcid.org/0000-0002-4856-7837>

References

- Andrews, S. M., Wilner, D. J., Zhu, Z., et al. 2016, *ApJL*, **820**, L40
 Astropy Collaboration, Price-Whelan, A. M., Sipőcz, B. M., et al. 2018, *AJ*, **156**, 123
 Astropy Collaboration, Robitaille, T. P., Tollerud, E. J., et al. 2013, *A&A*, **558**, A33
 Bai, X.-N., Ye, J., Goodman, J., & Yuan, F. 2016, *ApJ*, **818**, 152
 Balbus, S. A., & Hawley, J. F. 1991, *ApJ*, **376**, 214
 Banzatti, A., Pascucci, I., Edwards, S., et al. 2019, *ApJ*, **870**, 76
 Bradley, L., Sipőcz, B., Robitaille, T., et al. 2022, *astropy/photutils*: v1.5.0, Zenodo, doi:10.5281/zenodo.6825092
 Desch, S. J., & Turner, N. J. 2015, *ApJ*, **811**, 156
 Ercolano, B., Barlow, M. J., & Storey, P. J. 2005, *MNRAS*, **362**, 1038
 Ercolano, B., Barlow, M. J., Storey, P. J., & Liu, X.-W. 2003, *MNRAS*, **340**, 1136
 Ercolano, B., Koepferl, C., Owen, J., & Robitaille, T. 2015, *MNRAS*, **452**, 3689
 Ercolano, B., Mayr, D., Owen, J. E., Rosotti, G., & Manara, C. F. 2014, *MNRAS*, **439**, 256
 Ercolano, B., & Owen, J. E. 2010, *MNRAS*, **406**, 1553
 Ercolano, B., & Owen, J. E. 2016, *MNRAS*, **460**, 3472
 Ercolano, B., & Pascucci, I. 2017, *RSOS*, **4**, 170114
 Ercolano, B., Picogna, G., Monsch, K., Drake, J. J., & Preibisch, T. 2021, *MNRAS*, **508**, 1675
 Ercolano, B., Rosotti, G. P., Picogna, G., & Testi, L. 2017, *MNRAS*, **464**, L95
 Ercolano, B., Young, P. R., Drake, J. J., & Raymond, J. C. 2008, *ApJS*, **175**, 534
 Fang, M., Pascucci, I., Edwards, S., et al. 2018, *ApJ*, **868**, 28
 Fang, M., Wang, L., Herczeg, G. J., et al. 2023, *NatAs*, **7**, 905
 Gaia Collaboration, Smart, R. L., Sarro, L. M., et al. 2021, *A&A*, **649**, A6
 Gangi, M., Nisini, B., Antonucci, S., et al. 2020, *A&A*, **643**, A32
 Gorti, U., & Hollenbach, D. 2009, *ApJ*, **690**, 1539
 Gressel, O., Ramsey, J. P., Brinch, C., et al. 2020, *ApJ*, **896**, 126
 Gressel, O., Turner, N. J., Nelson, R. P., & McNally, C. P. 2015, *ApJ*, **801**, 84
 Harris, C. R., Millman, K. J., van der Walt, S. J., et al. 2020, *Natur*, **585**, 357
 Hunter, J. D. 2007, *CSE*, **9**, 90
 Jankovic, M. R., Owen, J. E., Mohanty, S., & Tan, J. C. 2021, *MNRAS*, **504**, 280
 Kamp, I., Tilling, I., Woitke, P., Thi, W.-F., & Hogerheijde, M. 2010, *A&A*, **510**, A18
 Koepferl, C. M., Ercolano, B., Dale, J., et al. 2013, *MNRAS*, **428**, 3327
 Lesur, G., Flock, M., Ercolano, B., et al. 2023, in *ASP Conf. Ser.* 534, *Protostars and Planets VII*, ed. S.-i. Inutsuka et al. (San Francisco, CA: ASP), 465
 Lesur, G. R. J. 2021, *A&A*, **650**, A35
 Mignone, A., Bodo, G., Massaglia, S., et al. 2007, *ApJS*, **170**, 228
 Najita, J. R., Carr, J. S., Strom, S. E., et al. 2010, *ApJ*, **712**, 274
 Nakatani, R., Hosokawa, T., Yoshida, N., Nomura, H., & Kuiper, R. 2018, *ApJ*, **857**, 57
 Owen, J. 2011, PhD thesis, Univ. of Cambridge
 Owen, J. E., Ercolano, B., Clarke, C. J., & Alexander, R. D. 2010, *MNRAS*, **401**, 1415
 Pascucci, I., Cabrit, S., Edwards, S., et al. 2023, in *ASP Conf. Ser.*, 534, *Protostars and Planets VII*, ed. S.-i. Inutsuka et al. (San Francisco, CA: ASP), 567
 Pascucci, I., & Sterzik, M. 2009, *ApJ*, **702**, 724
 Pascucci, I., Sterzik, M., Alexander, R. D., et al. 2011, *ApJ*, **736**, 13
 Picogna, G., Ercolano, B., & Espaillat, C. C. 2021, *MNRAS*, **508**, 3611
 Picogna, G., Ercolano, B., Owen, J. E., & Weber, M. L. 2019, *MNRAS*, **487**, 691
 Qi, C., Ho, P. T. P., Wilner, D. J., et al. 2004, *ApJL*, **616**, L11
 Rab, C., Weber, M., Grassi, T., et al. 2022, *A&A*, **668**, A154
 Robrade, J., & Schmitt, J. H. M. M. 2006, *A&A*, **449**, 737
 Simon, M. N., Pascucci, I., Edwards, S., et al. 2016, *ApJ*, **831**, 169
 Thi, W.-F., Woitke, P., & Kamp, I. 2011, *MNRAS*, **412**, 711
 van Boekel, R., Henning, T., Menu, J., et al. 2017, *ApJ*, **837**, 132
 Virtanen, P., Gommers, R., Oliphant, T. E., et al. 2020, *NatMe*, **17**, 261
 Wang, L., Bai, X.-N., & Goodman, J. 2019, *ApJ*, **874**, 90
 Weber, M. L., Ercolano, B., Picogna, G., Hartmann, L., & Rodenkirch, P. J. 2020, *MNRAS*, **496**, 223
 Weber, M. L., Ercolano, B., Picogna, G., & Rab, C. 2022, *MNRAS*, **517**, 3598
 Woitke, P., Kamp, I., & Thi, W.-F. 2009, *A&A*, **501**, 383
 Woitke, P., Kamp, I., Antonellini, S., et al. 2019, *PASP*, **131**, 064301
 Woitke, P., Min, M., Pinte, C., et al. 2016, *A&A*, **586**, A103